Ferromagnetic behavior of carbon nanospheres encapsulating silver nanoparticles

R. Caudillo,[1,*] X. Gao,[1] R. Escudero,[2] M. José-Yacaman,[1,3] and J. B. Goodenough[1]

[1]*Texas Materials Institute and Materials Science and Engineering, The University of Texas at Austin, 1 University Station C2201, Austin, Texas 78712-1063, USA*

[2]*Instituto de Investigaciones en Materiales, Universidad Nacional Autónoma de Mexico, Mexico, D.F., A. Postal 70-360 C.P. 04510, Mexico*

[3]*Department of Chemical Engineering, University of Texas at Austin, 1 University Station C0400, Austin, Texas 78712-1062, USA*

(Received 10 January 2006; revised manuscript received 30 October 2006; published 18 December 2006)

We report on the structure and magnetic properties of a silver and carbon nanocomposite. The as-synthesized nanocomposite consists of a matte-black powder composed of Ag nanoparticles encapsulated in carbon nanospheres (~10 nm diameter) that are interconnected in necklace-like structures. Magnetic measurements of the Ag and C nanocomposite, in its powder form, showed weak ferromagnetic behavior up to at least room temperature with a coercive field of 389 Oe at 2 K and 103 Oe at 300 K, from which we estimate magnetic ordering up to 425 K. However, pressing the Ag-C powder samples into tablets suppressed the ferromagnetism; the pressed samples instead exhibited diamagnetic behavior. Chemical analysis with EDS and trace metal analysis with ICP-MS indicated that there are no magnetic contaminants in the sample. Therefore, we attribute the ferromagnetism to the carbon nanospheres and propose a model for the observed magnetism. We also measured a pronounced peak in the magnetization between 50 and 90 K that was completely suppressed when measurements were made upon cooling; we attribute this peak to a first-order spin reorientation.

DOI: 10.1103/PhysRevB.74.214418 PACS number(s): 75.75.+a, 81.07.−b, 73.61.Wp, 81.05.Uw

I. INTRODUCTION

Recent reports of ferromagnetism in a variety of carbon materials have sparked renewed interest and intense research into the magnetic properties of carbon materials. Organic ferromagnets exhibiting spontaneous magnetization at room temperature were previously reported as early as 1987,[1–5] but these reports were received with skepticism due to the potential presence of magnetic impurities. As Miller[6] points out, for many magnetic polymers this skepticism proved to be a justified concern. More recently, for example, doubt was cast[7] on the intrinsic origin of the ferromagnetism with a 500 K Curie temperature previously reported in polymerized rhombohedral C_{60} (Ref. 8) after detailed chemical analysis revealed considerable iron content[9–11] in the carbon samples. For C_{60} compounds, ferromagnetism had also been reported in tetrakis(dimethylamino)ethylene-C_{60} (Refs. 12 and 13) and 3-aminophenyl-methano-C_{60}-cobaltocene[14] below 17 K and 19 K, respectively. On the other hand, ferromagnetic behavior up to 800 K had been reported for polymerized C_{60} that had undergone photoassisted oxidation.[15]

More recently there have been reports of ferromagnetism in proton-irradiated graphite,[16–20] nanographite,[21–25] graphite containing topographic defects,[26] negative curvature Schwarzite-like carbon nanofoams,[27–31] fullerene-related carbons,[11,32–36] microporous carbon,[37] as well as reports of a unique magnetic behavior of carbon nanohorns.[38] However, despite the growing number of carbon-based materials exhibiting ferromagnetic behavior, a clear explanation as to the origin of the magnetic behavior in these materials still needs to be developed. Some research suggests that hydrogen may play an important role in determining the magnetic properties of graphite.[19] On the other hand, the unique magnetic behavior in carbon nanohorns may be explained by the presence of adsorbed oxygen.[39] Still other research points to the importance of edge states[40] or topographic defects[26] or negative curvature[28] in the graphene sheets for determining magnetic properties. Kopelevich *et al.*[37] speculate that the ferromagnetism in microporous carbon may be attributable to graphitic fragments with positive or negative curvature.

In addition to the search for a more complete understanding of the mechanism of magnetic state formation in carbon and other *s*- and *p*-electron materials, the study of carbon nanomaterials with ferromagnetic properties is also driven by an enormous technological potential in nanotechnology, telecommunications, medicine, and biology. Exciting applications in medicine such as imaging blood flow with magnetic resonance imaging (MRI) machines, treatment of cancerous tumors, and enhanced brain scans have already been discussed.[41]

Here we present a class of "ferromagnetic" carbon consisting of carbon nanospheres encapsulating silver nanoparticles. The Ag-C material in its powder form exhibited ferromagnetic behavior up to at least room temperature, but pressing the powder suppressed the ferromagnetism and instead recovered the expected diamagnetic behavior for a bulk carbon sample. In addition, we measured a peak in the mass magnetization at low temperatures (50–90 K) that was suppressed when measured in the cooling direction. We propose a model that attributes the ferromagnetism to $(sp)^1$ localized spins in the carbon nanospheres and the peak to a first-order spin reorientation with a thermal hysteresis that suppresses the peak when measuring in the cooling direction. Alternatively, the peak may reflect an interparticle reorientation of magnetic carbon nanospheres.

II. EXPERIMENTAL DETAILS

A. Synthesis

The Ag-C nanocomposite was provided by Nanotechnologies, Inc.[47] Silver nanoparticles are synthesized by a

pulsed arc-discharge process and stabilized by carbon introduced into the system in the form of a hydrocarbon. Two cylindrical high-purity Ag electrodes are arc discharged in an inert gas flow such as argon. The arc discharge produces dramatic increases in temperature and pressure, vaporizing some of the Ag electrode and creating a plasma between the electrodes that is carried downstream by the gas flow. Rapid cooling causes Ag nanoparticles to nucleate and grow downstream. A hydrocarbon, e.g., acetylene or methane, is introduced into the process and results in a carbon coating on the Ag particles that stabilizes their size between 10 and 40 nm. The carbon-coated Ag nanoparticles are then collected downstream in the form of an easy to manipulate black powder. Large quantities of the material can be produced at high rates (many kgs per hour).

B. Structural characterization

The Ag-C sample was structurally and chemically characterized by scanning electron microscopy (SEM), energy dispersive spectroscopy (EDS), x-ray diffraction, and transmission electron microscopy (TEM), including both HRTEM (High Resolution TEM) and high angle annular dark field (HAADF) scanning TEM (STEM). Due to the dramatic differences in the magnetic properties between the unpressed powder samples and the pressed samples, we present a morphological characterization of both sample types. In addition, we demonstrate the ability to remove the Ag nanoparticles from the C nanospheres of the powder samples physically by electron irradiation in the TEM.

1. Unpressed powder samples

The powder sample was first characterized with a spherical aberration (C_s)-corrected JEOL JSM-7700F SEM. Figure 1 shows the SEM images of the Ag-C sample at three different magnifications. Here we can see that the sample consists of spherical particles with diameters of approximately 10–40 nm connected in necklace-like structures.

EDS chemical analysis detected both C and Ag in a weight % ratio of 70:30. Figure 2 (inset) shows an x-ray diffractogram of the sample confirming the presence of crystalline Ag. Peak broadening from x-ray diffraction gives an average Ag crystallite size of ~10 nm, agreeing well with SEM and TEM images. The absence of any x-ray diffraction peaks corresponding to a crystalline carbon phase, e.g., graphite, diamond, or fullerenes, might lead one to suggest that all of the carbon present in the sample is amorphous. However, Fig. 2 shows a typical TEM image of the sample clearly revealing crystalline order in the carbon surrounding a Ag nanoparticle. The carbon surrounding the Ag nanoparticles is not amorphous, but is instead graphitic although with an increased interplanar spacing of ~3.7 Å as compared to the 3.35 Å interplanar spacing expected for bulk graphite.

The very thin dimension of the graphitic carbon coating the Ag nanoparticles compared to the bulkier Ag nanoparticle substrate that it surrounds results in the x-ray diffraction signal from the Ag dominating; any diffraction from the graphitic carbon in the sample is lost in the diffracted x-ray signal. We also observe a large percentage of amorphous carbon in the sample, thus accounting for the larger weight % of C measured by EDS. However, the carbon sur-

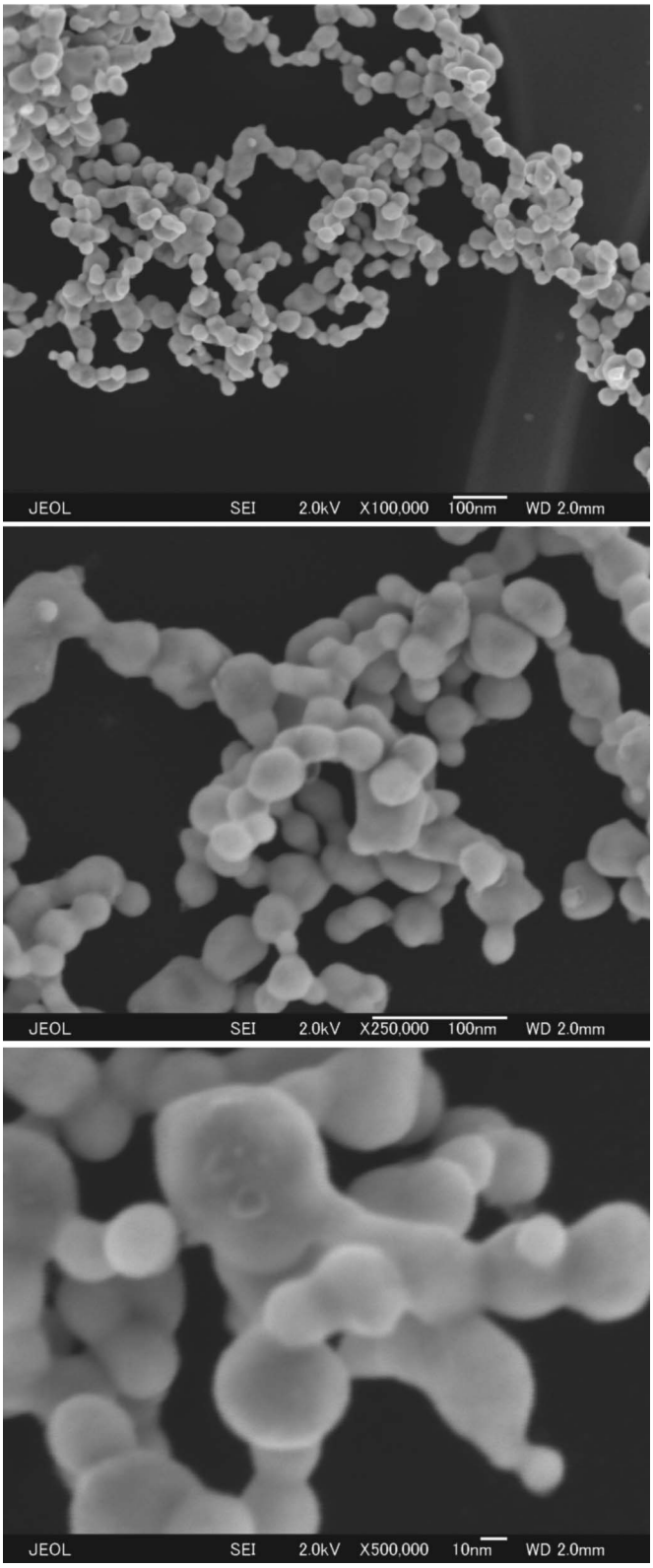

FIG. 1. SEM images of Ag-C sample at three different magnifications, clearly showing that the Ag-C powder consists of spherical particles connected in necklace-like structures.

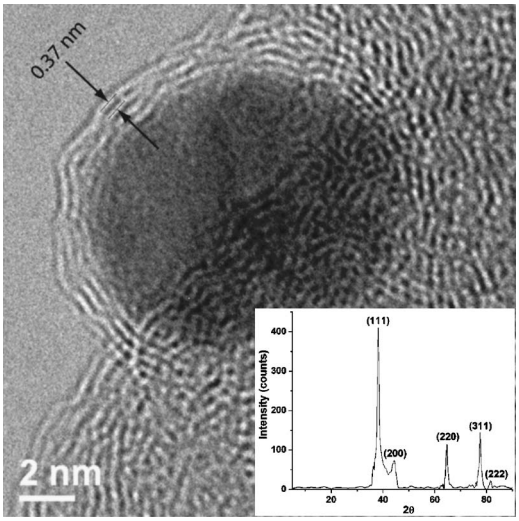

FIG. 2. HRTEM image showing a Ag nanoparticle (darker contrast) surrounded by graphitic carbon (C nanosphere) showing areas with an expanded interplanar spacing of 3.7 Å. Inset, x-ray diffractogram for Ag-C sample, indexed for the crystalline Ag cubic phase ($Fm\bar{3}m$). Peak broadening gives an average Ag crystallite size of ~10 nm.

rounding the Ag nanoparticles is always observed to be graphitic in the TEM. We refer to these graphitic shells encapsulating the Ag nanoparticles as carbon nanospheres.

2. Removal of Ag from the carbon nanospheres

The Ag can be removed from the C nanospheres either physically by a 200 keV electron beam in the TEM or chemically by acid treatment, e.g., with HCl or HNO_3. The physical removal of the Ag provides a better opportunity to study the structure of the C nanospheres and demonstrates their stability.

Figure 3 shows TEM images of the sample before and after physical removal of Ag by electron irradiation in the TEM. The Ag was removed by condensing the electron beam on the sample so as to achieve very high current densities at the sample, i.e., greater than 250 A/cm^2. Upon reaching a critical irradiation level, the Ag was observed to leave dramatically its carbon encasing and deposit immediately on the lacey carbon support of the TEM grid. The removal of Ag from the Ag-C nanocomposite left behind the C nanospheres intact, demonstrating their relative stability to the electron beam and revealing their spherical structure.

For chemical removal, the sample was treated with concentrated nitric acid and sonicated for 5 minutes. The product was then filtered with deionized water, dried with moderate heating, and then examined in the TEM. Figure 4 shows HAADF images comparing the differences in the samples after Ag removal by electron irradiation vs chemical extraction. In contrast to the images after physical removal of Ag by irradiation, the structure after chemical extraction appears more spongelike. Unlike the Ag removal by irradiation, the chemical treatment changes the structure of the carbon nanospheres; further measurements were not made on the chemically treated samples as their structure had been fundamentally altered.

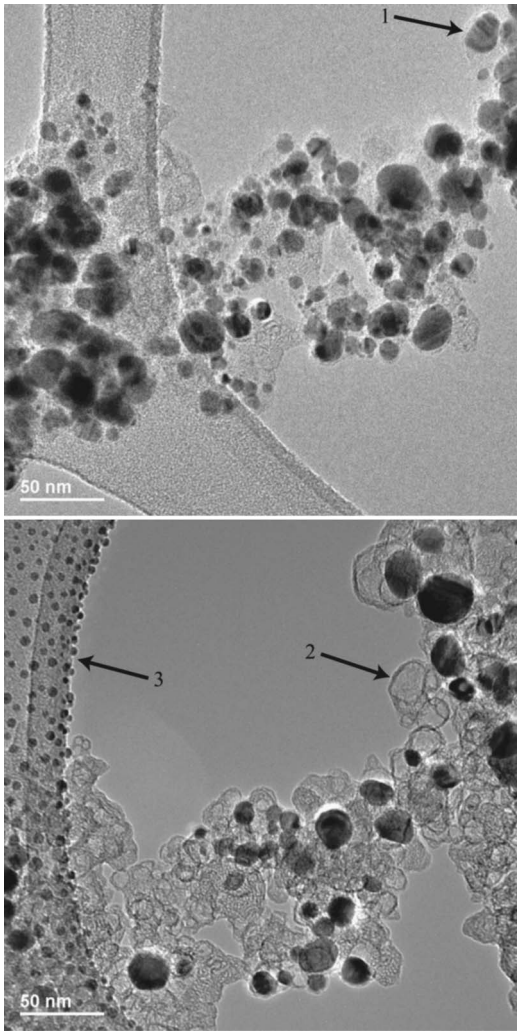

FIG. 3. TEM images showing the physical removal of Ag from carbon nanospheres by electron irradiation in the TEM. Top panel, Ag-C sample before Ag removal. Lower panel, same area after removal of Ag from the carbon nanospheres. Notice the smaller size and even distribution of the Ag nanoparticles deposited on the lacey carbon support after removal by intense irradiation (arrow 3) as well as the empty carbon nanospheres that remain after the Ag removal (arrow 2 is the same C nanosphere as arrow 1).

3. Pressed samples

Powder samples were pressed in a die into cylindrical tablets of ~5 mm diameter and ~2 mm height by applying up to 10 tons of pressure. All pressed samples (both 1-ton and 10-ton) exhibited a metallic sheen in contrast to the matte-black of unpressed powder samples. SEM characterization revealed that pressing with 10 tons changes the underlying structure of the nanocomposite by causing the coalescence of Ag nanoparticles into larger particles that show marked faceting (see Fig. 5) in contrast to the spherical geometries seen in the powder samples. On the other hand, samples pressed with ~1 ton of pressure showed no changes

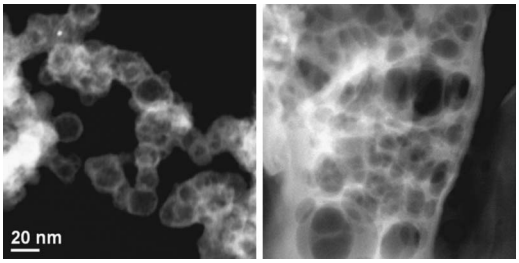

FIG. 4. HAADF STEM images showing the underlying carbon structure after silver removal by irradiation and by chemical extraction. Left panel, Ag removal by the *e*-beam in the TEM retains necklace-like structure of C nanospheres. Right panel, Ag removal by chemical treatment with nitric acid fundamentally changes the underlying carbon nanosphere structure to a spongelike carbon.

to their underlying morphology. Figure 6 shows an SEM image of a portion of a 1-ton-pressed sample at four different magnifications. The images clearly show that the carbon nanospheres are densely packed by the pressing process so as to form slabs. After pressing, they are less necklace-like, but they retain the morphology of carbon-encapsulated Ag nanoparticles, as is evident in the TEM image of Fig. 7 taken from the edge of a 1-ton-pressed sample.

C. Magnetic behavior

The magnetic properties of the Ag-C powder samples and 1-ton-pressed samples were analyzed with a Quantum Design superconducting quantum interference device (SQUID) magnetometer. Mass magnetization (M_{mass}) vs temperature (T) curves were measured for samples that were zero-field-cooled (ZFC) and field-cooled (FC). We define

$$M_{\mathrm{mass}} = M/(\text{total mass}),$$

where M is the magnetic moment and M_{mass} is the mass magnetization. In addition, FC measurements were taken in both directions, i.e., upon cooling and warming. The FC measurements taken in the cooling direction are referred to as FCC while those taken in the warming direction are referred to as FCW. For reference, ZFC measurements can only be taken in the warming direction. M_{mass} vs magnetic field (H), i.e., hysteresis curves, were also measured from 2 K up to 300 K, from which the coercive field (H_c) at different temperatures was obtained and then plotted vs T.

1. Ferromagnetic behavior of powder samples

Figure 8 shows the $M_{\mathrm{mass}}(T)$ behavior for both the powder and pressed samples. The three upper $M_{\mathrm{mass}}(T)$ curves correspond to a powder sample measured in the ZFC, FCC, and FCW modes already described. The only difference in $M_{\mathrm{mass}}(T)$ for the three measuring modes is in the peak that appears between 50 and 90 K. Also the $M_{\mathrm{mass}}(T)$ curves for the powder sample are positive and of greater magnitude than the $M_{\mathrm{mass}}(T)$ curve of the pressed sample, which is negative and corresponds to diamagnetic behavior.

In order to determine whether the positive $M_{\mathrm{mass}}(T)$ of the powder sample corresponds to ferromagnetic (or ferrimagnetic) behavior, M_{mass} vs H curves were measured at various temperatures. Figure 9 shows a selection of measured $M_{\mathrm{mass}}(H)$ curves for a sample measured at 2, 10, 50, 100, and 200 K. The upper left-hand inset of Fig. 9 is a close-up of the $M_{\mathrm{mass}}(H)$ curve at 10 K clearly showing a ferromagnetic hysteresis. The lower right-hand side inset is the corresponding $M_{\mathrm{mass}}(T)$ ZFC curve for the measured sample. Some differences in the M_{mass} values between the main panel $M_{\mathrm{mass}}(H)$ data and the inset $M_{\mathrm{mass}}(T)$ data for a given (H,T) are discussed in the context of a spin reorientation.

The H_c determined from $M_{\mathrm{mass}}(H)$ curves is also plotted vs T in Fig. 10; the $M_{\mathrm{mass}}(H)$ curves indicate a weak ferromagnetic behavior all the way up to 300 K with an $H_c = 389$ Oe at 2 K and an $H_c = 103$ Oe at 300 K. Furthermore,

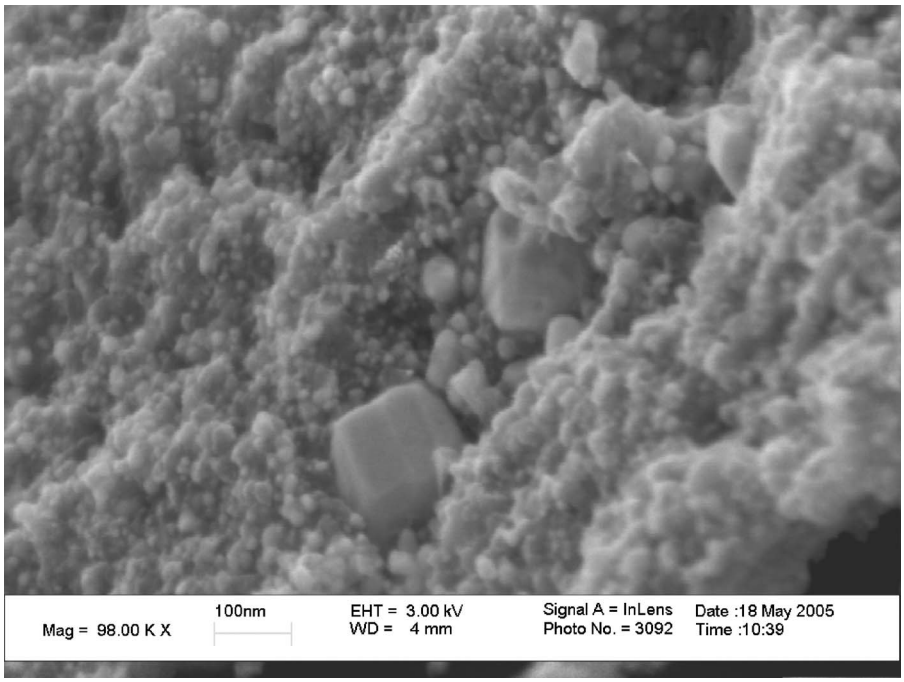

FIG. 5. SEM image of a 10-ton-pressed Ag-C sample showing the coalescence of some Ag nanoparticles into larger particles that show marked faceting.

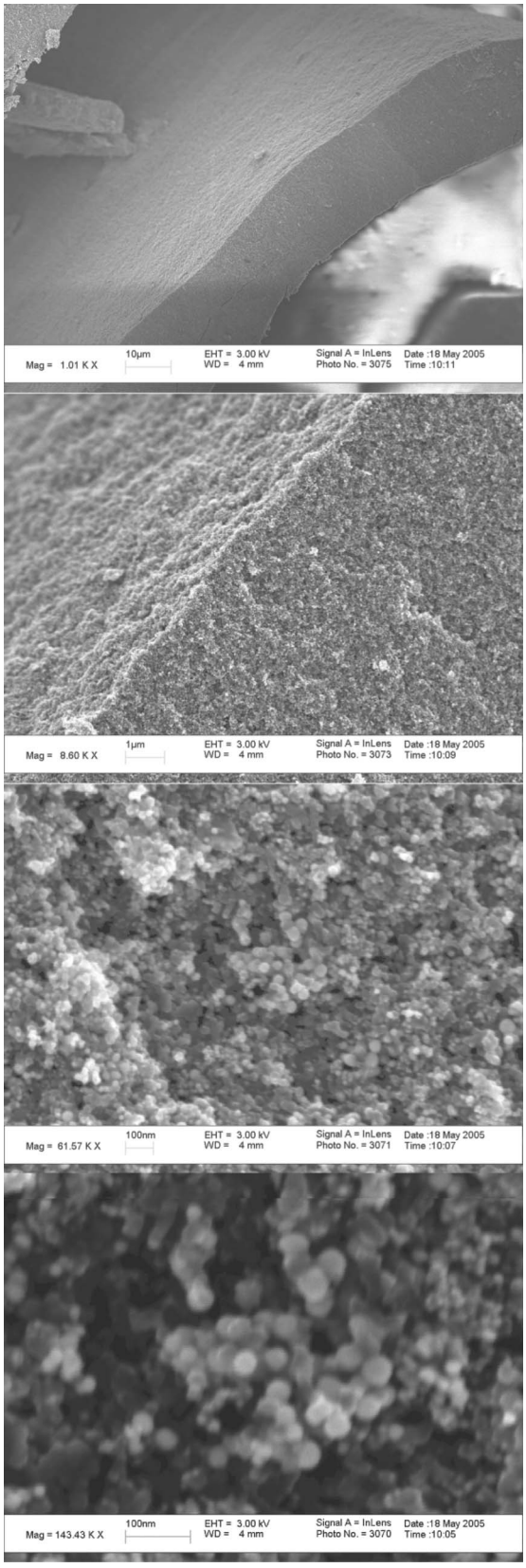

FIG. 6. SEM images of a 1-ton-pressed Ag-C sample at four different magnifications showing that the C-nanospheres densely pack to form slabs and still retain the underlying C-nanosphere morphology.

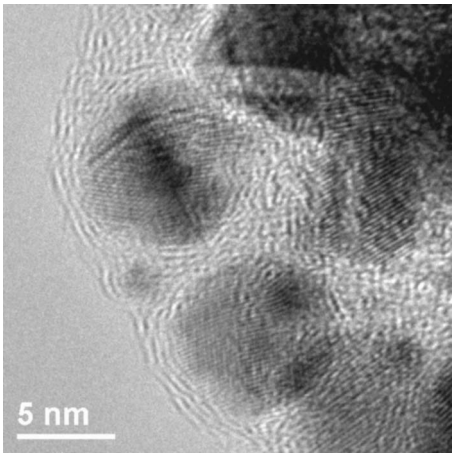

FIG. 7. TEM image of a 1-ton-pressed Ag-C sample showing that the morphology of the carbon-encapsulated Ag nanoparticles is maintained.

the $H_c(T)$ data (excluding the data giving the sharp increase in H_c at low T) can be fit to the mean-field approximation

$$H_c(T) = H_c(0)\sqrt{1 - \frac{T}{T_c}},$$

where the best fit is achieved for an extrapolated $H_c(0) = 190$ Oe and a $T_c = 425$ K, from which we estimate the presence of ferromagnetic behavior up to ~425 K (Fig. 10). The upturn in H_c at lower temperatures is discussed in the context of a spin reorientation.

Also of interest is the saturation behavior of the $M_{\text{mass}}(H)$ curves (Fig. 9). The curves taken at low temperatures, i.e., left of the $M_{\text{mass}}(T)$ peak, continue to increase to a higher M_{mass} while the higher-temperature curves, i.e., right of the peak, appear to saturate at a lower H and show a downturn in M_{mass} with increasing H beyond saturation. The downturn in

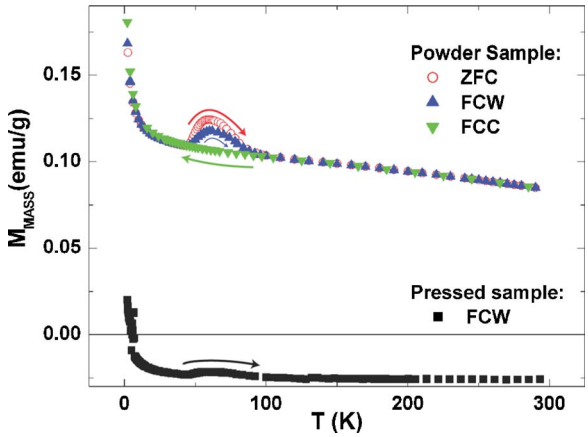

FIG. 8. (Color online) $M_{\text{mass}}(T)$ curves for powder Ag-C samples (upper) and pressed Ag-C samples (lower) measured in a field of 1.0 T. Arrows indicate whether the measurement was made upon cooling or warming.

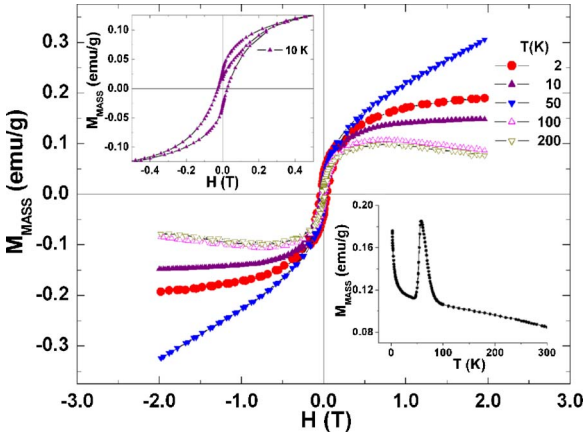

FIG. 9. (Color online) Selected $M_{\text{mass}}(H)$ curves for a ZFC powder sample. Upper left inset, close up of $M_{\text{mass}}(H)$ curve at 10 K clearly showing ferromagnetic hysteresis. Lower right inset, corresponding $M_{\text{mass}}(T)$ ZFC curve.

the $M_{\text{mass}}(H)$ curves suggests that there is a diamagnetic component present in the sample that begins to dominate at higher H once the ferromagnetic component has saturated.

2. Diamagnetic behavior of pressed samples

The lower curve in Fig. 8 shows the $M_{\text{mass}}(T)$ behavior for a sample pressed with ~1 ton of pressure. The pressed sample is no longer ferromagnetic, but instead shows diamagnetic behavior above 5 K with a sharp tail at low T that gives a positive M_{mass} below 5 K. In addition, because diamagnetism and ferromagnetism can coexist,[42] Figure 11 shows $M_{\text{mass}}(H)$ curves that clearly demonstrate the absence of ferromagnetic hysteresis in the pressed samples and thus the complete transition to diamagnetic behavior with isolated paramagnetic spins in the pressed samples. Furthermore, the diamagnetic behavior strongly suggests that the ferromagnetic behavior of the powder samples is intrinsic to the Ag-C sample and cannot be explained by magnetic impurities since the pressed sample and the powder sample consist of the same materials.

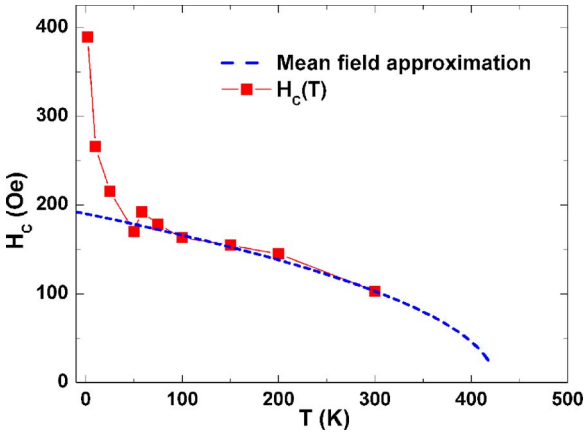

FIG. 10. (Color online) H_c calculated from $M_{\text{mass}}(H)$ curves plotted vs T showing ferromagnetic behavior up to 300 K. Mean field approximation giving a $T_c \approx 425$ K.

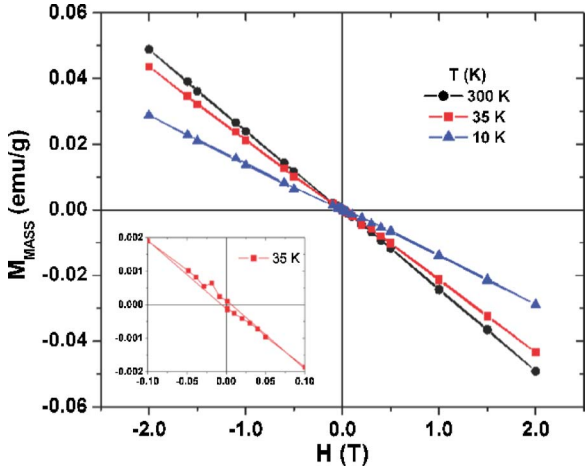

FIG. 11. (Color online) Selected $M_{\text{mass}}(H)$ curves for a pressed sample at 10 K, 35 K, and 300 K, clearly showing the absence of ferromagnetic hysteresis and complete transition to diamagnetic behavior in the pressed samples. Inset, magnified view of $M_{\text{mass}}(H)$ curve at 35 K showing the diamagnetic behavior at low fields.

The diamagnetic M_{mass} ($T > 100$ K) in Fig. 8 corresponds to a mass susceptibility of $\sim -2.6 \times 10^{-6}$ emu/g, which is within the range of the diamagnetic susceptibility of nearly all known carbon allotropes, which exhibit diamagnetic susceptibility in the range of $\chi = -(10^{-5} - 10^{-7})$ emu/g.[29] Linear fits to the $M_{\text{mass}}(H)$ curves of Fig. 11 also give a mass susceptibility approaching $\sim -2.6 \times 10^{-6}$ emu/g. Therefore, pressing the sample recovers the diamagnetic behavior expected for bulk carbon as well as suppressing the peak in the $M_{\text{mass}}(T)$. We attribute the low-T tail (below 5 K) to retention of isolated paramagnetic spins in the carbon mass.

3. Corrected mass magnetization for powder samples

As previously discussed, from Fig. 9 we deduce the presence of both a diamagnetic and weak ferromagnetic component in the powder samples. If we assume that the diamagnetic component in the powder samples responsible for the downturn in the $M_{\text{mass}}(H)$ curves has the same magnitude as the diamagnetic component in the pressed samples, we can use the diamagnetic susceptibility of the pressed samples,

$$\chi_{\text{dia}} = -2.6 \times 10^{-6} \text{ emu/g},$$

to correct the $M_{\text{mass}}(H)$ curves of the powder samples of Fig. 9. Accordingly, we define a corrected magnetization,

$$M_{\text{corr}}(H) = M_{\text{mass}}(H) - \chi_{\text{dia}} H,$$

for the ferromagnetic component of the powder samples. Figure 12 shows $M_{\text{corr}}(H)$. The correction eliminates the downturn in the magnetization observed in Fig. 9, thus supporting that the diamagnetic component in the pressed sample is about the same as that in the powder sample. Furthermore, we now see that for $T \geq 100$ K the M_{corr} nearly saturates in an applied $H = 2$ T with an $M_s \rightarrow 0.14$ emu/g. For lower T, the M_{corr} does not saturate in an applied $H = 2$ T, especially for temperatures corresponding to the $M_{\text{mass}}(T)$ peak where it reaches 0.35 emu/g at 2 T.

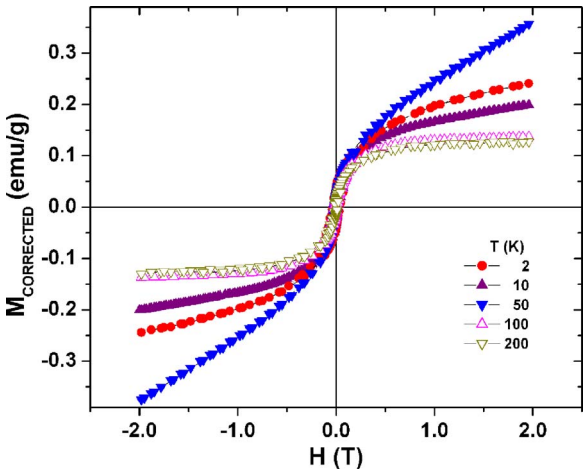

FIG. 12. (Color online) Corrected mass magnetization, $M_{\mathrm{corr}}(T)$, for powder Ag-C samples showing a near saturation of the magnetization for $T \geq 100$ K.

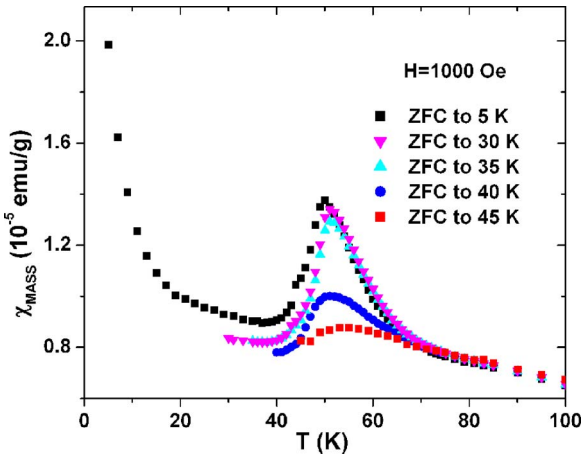

FIG. 13. (Color online) Mass susceptibility $\chi_{\mathrm{mass}}(T)$ for powder Ag-C samples ZFC to different temperatures, showing a thermal hysteresis that results in the peak being suppressed for samples that are not sufficiently cooled.

4. Peak in the mass magnetization and spin reorientation

Our data are consistent with a first-order spin reorientation with a critical temperature (T_m) that varies only a little between nanospheres, but exhibits a thermal hysteresis. The critical temperature upon warming is $50\ \mathrm{K} < T_{m\uparrow} < 90\ \mathrm{K}$; upon cooling, the critical temperature occurs at a lower temperature. In order to test this deduction, we measured the ZFC curves for samples cooled to different temperatures to see at what lower temperature the peak in $M_{\mathrm{mass}}(T)$ appears. The result, shown in Fig. 13, clearly identifies the interval $30\ \mathrm{K} < T_{m\downarrow} < 40\ \mathrm{K}$ for the critical temperature on cooling in zero field. In addition, there appears to be a time dependence of the spin reorientation that makes the transition sluggish upon cooling in an applied magnetic field. If an applied magnetic field inhibits the spin reorientation, it would slow it down to broaden the peak in the FCC measurement to where it is not visible. This situation would occur if the higher temperature spin orientation were favored by an applied magnetic field.

D. Trace metal analysis

The presence of the observed magnetic behavior in a sample containing only Ag and C is highly unusual since Ag and bulk carbon are diamagnetic. For this reason, the sample was examined for traces of magnetic contaminants with a micromass platform quadrapole inductively coupled plasma mass spectrometer (ICP-MS) with a hexapole collision and/or reaction cell and a single Daly-type detector.

Mass spectrometry measurements were done on milligram samples of the Ag-C sample extracted with concentrated HNO_3 and sonicated with ultrasound for at least 20 minutes. The solutions were then diluted to appropriate levels for comparison to calibrated standard solutions. Two solutions were analyzed in detail, along with a method blank consisting of the concentrated HNO_3 sonicated without the sample and diluted and prepared for analysis in the same way as the two sample solutions. Samples were scanned for all possible elements and quantitatively analyzed for the following elements: Li, B, Na, Mg, Al, Si, P, K, Ca, V, Cr, Mn, Fe, Co, Ni, Cu, Zn, As, Se, Rb, Sr, Mo, Ag, Cd, Sn, Sb, Cs, Ba, La, Ce, Pb, Bi, Th, and U.

Table I shows the summary of the quantitative ICP-MS analysis. Both sample solutions gave strong peaks for Ag in the ppm range, indicating that the Ag was dissolved out of the Ag-C sample and suggesting that other metals present in the sample should also have been dissolved into the solution. The two sample solutions showed only some metal contaminants in the ppb range with all other elements falling below the detection limit (BDL). Of the elements detected in the ppb range, only one of them, Cu^{65}, was detected in both sample 1 and 2. Cu was less than 100 ppb above the method blank and is usually not magnetic. Cr was detected in one sample solution (350 ppb above the method blank) and was BDL in the other sample solution. The other elements listed in Table I were only detected in one sample and were all present in greater amounts in the method blank. Thus the only possible magnetic contaminant detected, Cr, was only found in one of the sample solutions and was only 0.1% of the amount of Ag detected in the solution; therefore it cannot explain the observed magnetic behavior. These results support that the magnetism being reported is indeed coming

TABLE I. Summary of ICP-MS elemental analysis [below detection limit (BDL)].

Element	Method blank (ppb)	Sample 1 (ppb)	Sample 2 (ppb)
^{52}Cr	21.7	BDL	373
^{60}Ni	1449	BDL	161
^{63}Cu	22.4	88.1	113
^{65}Cu	22.7	85.3	BDL
^{109}Ag	BDL	683135	316706
^{114}Cd	BDL	64.0	BDL
^{120}Sn	BDL	3.46	BDL
Other		BDL	BDL

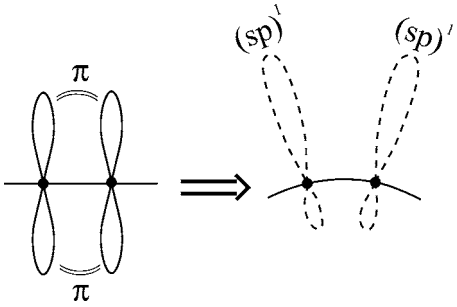

FIG. 14. Schematic representation showing the transition from p_π delocalized spins in a planar graphene sheet toward $(sp)^1$ localized spins in a curved graphene sheet.

from the Ag-C sample and not from magnetic contaminants present in the sample.

III. DISCUSSION

A model accounting for the observed magnetic behavior must not only be able to explain how spins are localized in the Ag-C sample, but also what type of magnetic interaction exists between the localized spins in order to give a net magnetic moment and the observed ferromagnetic behavior. Localization of spins in Ag is unlikely since Ag has a full $4d^{10}$ shell and one $5s^1$ electron that is delocalized in a broad, half-filled band that gives metallic conduction. Therefore, the localized spins and the ferromagnetic behavior must be coming from the carbon surrounding the Ag nanoparticles. In order to understand how the spins are being localized in the carbon, we must first have an understanding of the structure of the carbon coating the Ag nanoparticles.

As seen in Figs. 1–4, the carbon forms necklace-like structures comprised of interconnected spheres. The spheres are nested, closed carbon cages of a graphene nature that encapsulate the Ag nanoparticles. For example, Fig. 2 shows a carbon nanosphere consisting of four nested, closed carbon cages.

What is most important about the structure for a model of the ferromagnetism is the curvature of the nanospheres. In graphite, sp^2+p_π bonding gives metallic behavior from itinerant p_π electrons both in the *ab* plane and in narrow *c*-axis dispersion bands. Introducing a curvature to graphene planes changes the sp^2+p_π bonding towards sp^3 hybridization as found in Si, but with a half-filled $(sp)^1$ orbital extending out from the curved graphene sheet (see Fig. 14). For a large curvature of the graphene sheets, the *s* character of the (sp) hybrid orbital is large so that extension of the orbital is small on the interior of the graphene layers, i.e., towards the center of the nanosphere. Consequently, for a large curvature these half-filled orbitals have only a small overlap with like orbitals on their carbon near neighbors in the plane and, as discussed below, between half of the carbon across planes. Thus the curvature reduces the overlap of the half-filled orbitals perpendicular to the surface of the carbon sheets from that of the p_π orbitals of flat sheets until, at a critical curvature, the electrons in these orbitals become localized with a spin $S=1/2$ in the absence of strong interplane interactions.

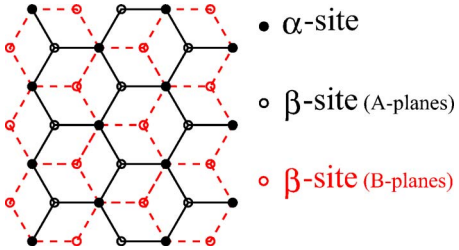

FIG. 15. (Color online) Schematic illustration showing the α and β sites in graphite.

Across planes, the situation is more complex as there exist two distinct carbon sites in graphite. Due to the *ABAB* *c*-axis stacking of carbon planes in graphite, there are carbon α sites with carbon neighbors directly below and above and carbon β sites without carbon neighbors directly below and above (Fig. 15). Thus half of the carbon atoms are in α sites that form chains of C atoms along the *c* axis while the other half are in β sites with no carbon neighbors directly above or below.

Whereas the curvature reduces the in-plane π bonding to where the spins on the β sites are localized, the interplane bonding between α-site C atoms remains strong enough to give a one-dimensional (1D) itinerant-electron band. If the 1D band remains half-filled, we should expect an antiferromagnetic coupling between the β-site spins through the α-site 1D band. However, a smaller work function for silver than for graphite, $\Phi_{Ag}<\Phi_C$, means that electrons are donated from the Ag nanoparticles to the C nanospheres. Since the correlation splitting U of the $(sp)^1$ and $(sp)^2$ states at the β sites is larger than the splitting of the two-electron and three-electron bonds of the α sites, the Ag can be expected to donate electrons to the 1D α-site bands to make them ca. 3/4-filled with a spin of $0.5\mu_B/C_\alpha$. As shown schematically in Fig. 16, the dominant virtual charge transfer is from an α chain to a β site, and the Pauli exclusion principle only allows transfer of electrons with a spin opposite to the spin on a β site. Therefore, we anticipate an antiferromagnetic coupling between the α-site and β-site spins to give a net ferrimagnetic moment of ca. $0.25\mu_B/C$ for the powder samples.

This model is supported by the TEM image in Fig. 2 where we see that the interplanar spacing of the carbon sheets surrounding the Ag nanoparticles is ~3.7 Å, which is

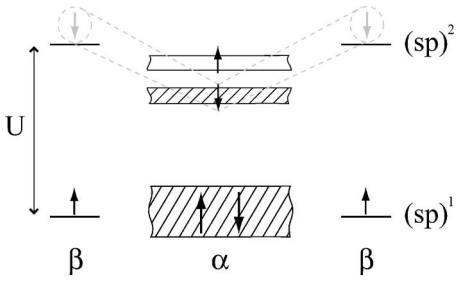

FIG. 16. Schematic illustration of the ferromagnetic superexchange interaction between β sites through a strongly correlated 3/4-filled α band. Here $(sp)^1$ indicates a half-filled (sp) orbital and $(sp)^2$ indicates a filled (sp) orbital, and U is the correlation splitting of the $(sp)^1$ and $(sp)^2$ states.

greater than the 3.35 Å spacing of graphite. The larger C-C distance between the α-site C atoms is consistent with the introduction of antibonding electrons that, in essence, transforms two-electron bonding orbitals to three-electron bonds with localized antibonding-electron spins. From the virial theorem, as has been argued elsewhere,[45] the transition from spin-paired to strongly correlated antibonding electrons would increase the separation of the α-site C along a 1D chain, as we observe in our TEM images of the powder samples.

Flattening of the graphitic sheets would restore graphite p_π bonding to eliminate even the localized β spins; however, our structural characterization indicates that this is not the case for the 1-ton-pressed samples since the curvature is maintained (see Fig. 7) in the graphene sheets surrounding the Ag nanoparticles. Instead this pressure appears to increase the C-C bonding between nanospheres and, more importantly, shorten the C-C interplanar spacing, thus broadening the 1D α-site bands and pairing antiparallel the β-site spins. This would revert the system to the diamagnetic behavior expected for a bulk Ag and C samples, which we indeed observe in Fig. 8 and Fig. 11 for the pressed samples.

The peak in the $M_{\text{mass}}(T)$ data can be explained by a spin reorientation. The only difference in the FCW and ZFC $M_{\text{mass}}(T)$ curves of Fig. 8 for the powder sample is in the magnitude of a peak found in the interval $50\ \text{K} < T < 90\ \text{K}$. The peak is only observed for measurements made in the warming direction (ZFC and FCW); it is completely suppressed for measurements made in the cooling direction (FCC). Also the magnitude of the ZFC peak is always slightly greater than the FCW peak.

A similar peak in carbon nanohorns has been reported by Bandow *et al.*[39] and was attributed to adsorbed oxygen. Although there are similarities between the $M_{\text{mass}}(T)$ peak of the carbon nanosphere powder samples and the peak in the carbon nanohorn samples, the peak we observe cannot be explained by the presence of oxygen because of the thermal hysteresis and suppression of the peak when measuring in the cooling direction. There are magnetic transitions associated with solid oxygen within the peak temperature interval,[43,44] but they are second- order and thus are always observed at the same temperature whether measurements are made upon warming or cooling (no thermal hysteresis). Therefore, the presence of oxygen cannot explain the observed peak in the carbon nanosphere sample; instead, we propose an explanation for the observed peak based on a first-order spin reorientation.

Both the $M_{\text{mass}}(T)$ and $M_{\text{corr}}(H)$ behavior suggest that the sample exhibits a spin reorientation at the temperature corresponding to the peak. A spin reorientation occurs when there is a change in the site easy-magnetization axis. Where the spins reorient their direction, the spin system becomes more plastic, which allows for a larger M in an applied H. In a second-order transition, the site anisotropy energy goes smoothly through zero; but in a first-order transition, the anisotropy energy goes to a minimum, but remains finite. A displacive structural change would accompany a first-order transition.

A spin reorientation is thus able to explain the complete suppression of the peak upon cooling in a magnetic field (FCC curve in Fig. 8), as well as the smaller thermal hysteresis upon cooling in zero field shown in the ZFC curves of Fig. 13. In addition, the $M_{\text{corr}}(H)$ curves measured at temperatures corresponding to the $M_{\text{mass}}(T)$ peak, where the spin system is more plastic, showed a greatly increased saturation M_{corr} that is consistent with a spin reorientation (see Fig 12). For example, at 50 K, $M_{\text{corr}}(H)$ is still increasing strongly at an H of 2 T with a $M_{\text{corr}} \approx 0.35$ emu/g.

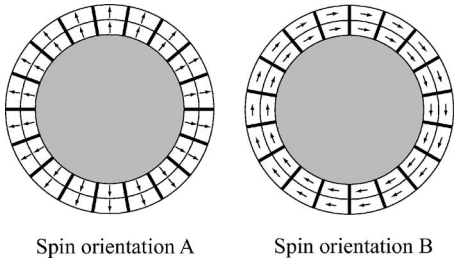

FIG. 17. Schematic illustration showing two possible spin orientations of localized $(sp)^1\beta$ spins separated by itinerant α sites. Orientation A corresponds to spins oriented along the (sp) orbital axis, while orientation B corresponds to spins tangential to the spherical surface.

A spin reorientation is also supported by the increase in H_c for temperatures below the $M_{\text{mass}}(T)$ peak (see Fig. 10). We expect different spin orientations to lead to a difference in the nature of the domain structure and thus in the $M_{\text{corr}}(H)$ behavior and the H_c. Apparently, the lower temperature orientation has a higher saturation magnetization at a higher field (Fig. 12) as well as a larger H_c that increases more rapidly with temperature, giving an upturn in the low-temperature H_c (Fig. 10).

Furthermore, we attribute the difference in the magnetization data between the main panel and the lower right-hand side inset of Fig. 9 to the time dependence of the spin reorientation. At 50 K the $M_{\text{mass}}(H)$ data were taken over a much longer time than the $M_{\text{mass}}(T)$ measurements; the spin system has thus become more plastic, resulting in a $M_{\text{mass}}(50\ \text{K}) > M_{\text{mass}}(2\ \text{K})$ at $H=1$ T in the main panel, whereas in the lower right-hand side inset $M_{\text{mass}}(2\ \text{K}) > M_{\text{mass}}(50\ \text{K})$.

Figure 17 shows the suspected spin orientations, where orientation A corresponds to spins oriented parallel to the (sp) orbital axis, i.e., perpendicular to the carbon nanosphere surface, and orientation B corresponds to spins oriented perpendicular to the orbital axis, i.e., tangential to the carbon nanosphere surface. As deduced above for a 3/4-filled α band, a net moment of $0.25\mu_B$/C atom is expected. However, from Fig. 17 we see that the spin orientations and the spherical geometry of the carbon nanospheres results in no net magnetic moment in the absence of an external magnetic field. However, once domain walls have been introduced by the application of a magnetic field, a remnant magnetization and a coercivity can be expected.

Figure 18 shows how both spin orientations result in a net ferromagnetic moment in an external magnetic field. For orientation A, more spins align parallel to the external field by forming a Bloch wall, which is shown in Fig. 18 as an idealized Bloch wall across the equator of the nanosphere. The net ferromagnetic moment increases from the equator to the

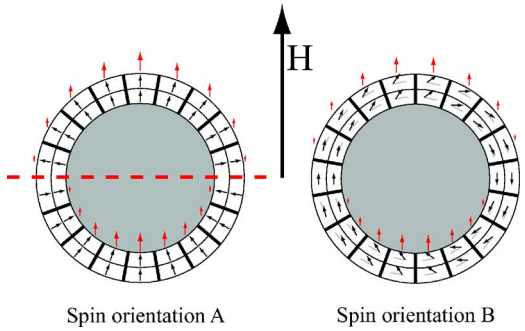

FIG. 18. (Color online) Schematic illustration showing spin orientation A and B in an applied external field H. Orientation A achieves a net ferromagnetic moment by the formation of a Bloch wall (dashed red line) in addition to spin-canting (not shown). Orientation B achieves a net ferromagnetic moment by spin canting. The small red arrows shown on the outer and inner surface of the carbon shells are schematic representations of the net ferromagnetic moment and show an increasing ferromagnetic moment for both orientations as one approaches the poles.

poles due to an increasing component of the preferred spin orientation lying in the direction of the external field. In addition, spins canting away from the preferred spin orientation, i.e., parallel to the (sp) orbital axis, may also contribute to the net moment. Spin orientation B achieves a net moment by canting its spins away from the spherical surface in the direction of the external field. For this case, the net ferromagnetic moment increases from the equator to the poles because of an increasing torque exerted by the external field on the spins. Both orientations do not allow complete alignment of the β spins in an applied H, so that the net moment for each spin orientation is less than the $0.25\mu_B$/C atom previously calculated.

If the local net moment $\mu=0.25\mu_B$/C atom, then for spin orientation A it can be shown that the net moment for a carbon nanosphere is approximately

$$\mu_A = \int_S \mu\cos(\phi)dS = \frac{2r^2\int_0^{\pi/2}\mu\cos(\phi)\sin(\phi)d\phi\int_0^{2\pi}d\theta}{4\pi r^2}$$

$$= 0.5\mu = 0.125\mu_B/\text{C atom}$$

or 50% of the $\mu=0.25\mu_B$/C, not including any canting of the spins away from the (sp) orbital axis, which would further increase the net moment. On the other hand, it is not possible to calculate the net moment for spin orientation B without knowing the degree of spin canting out of the plane. Although it is difficult to determine from these considerations which spin orientation occurs at low and high temperature, nevertheless, our experimental data support a spin reorientation that causes a peak in the $M_{\text{mass}}(T)$ curves upon warming but not upon cooling, an upturn in the H_c at low temperatures that corresponds to a more difficult spin reversal of the low-temperature spin orientation, and a difference in saturation magnetizations at temperatures below and above the spin reorientation temperature.

The ferromagnetic areas appear to be separated by domain walls as in any ferromagnet. The motion of these walls in an applied field H allows the tracing out of an M-H hysteresis loop. However, bending of the spins into the direction of the applied H field would be resisted by the magnetocrystalline anisotropy, which is expected to be different for each spin orientation. Therefore, although it is not possible to determine which of the suspected spin orientations is favored at the lower or higher temperatures, it is apparent that the low-temperature orientation results in a higher H_c that increases more rapidly with decreasing temperature. Also, the low temperature orientation does not allow for full ferromagnetic alignment of the spins in an $H=2$ T, suggesting a stronger magnetocrystalline anisotropy. Rotation of the spins from parallel to perpendicular to the orbital axes would occur at a temperature where the net site anisotropy becomes small and the spins are more easily aligned in the direction of the applied field; but the interatomic exchange field does not change sign. Such a spin reorientation would result in a peak in the $M_{\text{mass}}(T)$, which is indeed observed.

On the outer surface of the carbon nanosphere the $(sp)^1$ orbital will be a reactive surface state so long as there is no interaction with a neighboring nanosphere or an adsorbed species. In the graphene layers below the surface, the localized $(sp)^1$ electrons appear to be sterically protected from adsorbed species, thus giving the observed ferrimagnetic behavior in the powder samples even if the surface states are all spin-paired with a surface species or a neighboring nanosphere. With three concentric carbon nanospheres and $\mu=0.125\mu_B$/C atom about each Ag particle (assuming orientation A), we can estimate a magnetization $M_{\text{corr}} \approx 0.6$ emu/g, which is sufficient to account for the observed magnetization M_{corr}.

The reactive states on a carbon nanosphere surface provide the C-C bonding between nanospheres needed to form the robust necklace-like structures observed in the powder samples. The other reactive surface sites may be satisfied by chemisorbed species, e.g., the oxygen detected in small quantities with EDS and/or hydrogen from adsorbed H_2O. Satisfaction of the active surface sites would explain why, under the pressure of a die, the carbon nanosphere necklaces can form slabs of densely packed nanospheres that are fragile enough that they can relatively easily be mechanically broken back down into the original carbon nanosphere necklace-like structures of the Ag-C powder. That is, if the electrons on the surface of the C nanospheres remained as reactive sites, then one would expect a chemical bond between pressed C nanospheres and much more robust pressed samples. However, since this is not the case, it appears that the C-C bonding between nanospheres needed to form the necklace-like structures occurred during the synthesis process and the remaining exposed surface sites became satisfied by chemisorbed species, such as the oxygen and water present in the air to which the samples were exposed immediately after synthesis and during their handling.

This model accounts qualitatively for the presence of a diamagnetic and a weak ferrimagnetic contribution to the magnetic susceptibility as is signaled by the magnetic measurements in Fig. 9. It also predicts a magnetic-ordering temperature and weak ferrimagnetism that is dependent on elec-

tron transfer from the Ag particles to the α-site C chains. Although the model allows for a reorientation of the spin axis relative to the (sp) orbital axis, our data do not provide an unambiguous identification of which spin orientation is favored at the lowest temperatures. Nevertheless, we would expect spin orientation B to be favored at lower temperatures since this orientation is stabilized by magnetostatics.

While we have principally considered intraparticle interactions, e.g., spin orientation relative to the (sp) orbital axis, it may be that the interparticle interactions, i.e., between nanospheres, are of importance in explaining some of the magnetic behavior of these samples. Then the peak in the $M(T)$ may be associated with an interparticle spin reorientation between carbon nanospheres or with a transition from a superparamagnetic to a blocked state.

IV. CONCLUSIONS

Carbon can be present in many different forms, each exhibiting drastically different properties. Carbon nanostructures, such as fullerenes, onions, and CNTs have generated much scientific research and are already being used in numerous applications. More recently, carbon nanostructures, such as carbon nanofoam, have sparked interest in carbon materials that possess ferromagnetic properties. The carbon nanostructures presented here appear to be one such material.

We conclude that by increasing the curvature of a graphite sheet to beyond a critical value, it is possible to generate reactive, half-filled $(sp)^1$ orbitals projecting from the outer surface and localized $(sp)^1$ spins below the surface. The reactive, localized spins on the surface may be spin-paired by adsorbed species or by C-C bonding with neighboring nanospheres. The localized $(sp)^1$ spins below the surface occur at β sites and interact within a graphene sheet through a strongly correlated itinerant-electron band at α sites that form carbon chains along the c axis.

A difference in work functions between Ag and C results in the Ag nanoparticle donating electrons to the carbon nanosphere α band so that it becomes more than half-filled. The magnetic interaction between the localized spins at the β sites is through a more than half-filled α band that gives a ferromagnetic alignment of the β spins through a spin-polarized α band with an antiferromagnetically aligned net moment that is less than the moment on the β sites. Therefore the interaction between the α and β sites is ferrimagnetic with a magnetic ordering above room temperature.

Pressure is assumed to shorten the C-C bonds of the α-site chains, which suppresses the spin-polarization of the α-site antibonding electrons and leaves only antiferromagnetic coupling between the β-site spins. As a result, the diamagnetism of the carbon dominates the susceptibility of the pressed samples.

We believe this finding opens the door to tailoring the curvature of carbon nanospheres encapsulating a metallic nanoparticle core for a variety of applications. For example, carbon is a biologically friendly material and Ag, even when sterically stabilized, has been shown to have antimicrobial properties and even shows the potential to inhibit HIV.[46] In this light, a ferromagnetic carbon coating could prove very useful in drug delivery, or even guided drug delivery where a magnetic field, e.g., from an MRI, is used to guide the encapsulated material to a specific location in the human body. Furthermore, there seems to be no reason why the synthesis could not be extended to include other metals within the ferromagnetic carbon nanospheres, thus opening many new possibilities.

More fundamentally, this paper proposes a model for ferromagnetic interactions in graphitic carbon materials. While there are various models for the localization of spins in carbon materials, there are very few models for the magnetic interaction between such localized spins capable of explaining the recently observed ferromagnetic behavior in a variety of carbon materials.

V. OBSERVATIONS

Recently, a significant number and variety of carbon materials with ferromagnetic properties have been reported. Unlike the negative curvature carbon nanofoams, our material contains Ag nanoparticles that play the role of electron donors to α-site bands that are spin polarized and give a net ferrimagnetic moment from α and β sites. We note here that we have used a model that is not dependent on negative curvature regions in the carbon. Although one might expect such regions to exist at the necks of neighboring carbon nanospheres in necklace-like structures, from Fig. 4 (left-hand panel) we can find no evidence of such negative curvature regions in our material; instead we clearly observe spherical carbon shells joined by C-C bonding.

ACKNOWLEDGMENTS

The authors thank Kevin Walter, Jim Bryant, and Nanotechnologies for providing the Ag-C material, Jose Luis Elechiguerra for discussion and experimental work on the chemical removal of Ag by acid treatment, John Lansdown for help with the ICP-MS analysis, Ronald Dass and Jose Reyes Gasga for helpful discussion, Darshan Sachde for laboratory help, and Alejandro Diaz-Ortiz for help with the preparation of this paper. One of the authors (R.C.) thanks UT-Austin for support.

*Electronic address: rcaudillo@mail.utexas.edu

[1] J. B. Torrance, S. Oostra, and A. Nazzal, Synth. Met. **19**, 709 (1987).

[2] A. A. Ovchinnikov and V. N. Spector, Synth. Met. **27**, B615 (1988).

[3] K. Murata, H. Ushijima, H. Ueda, and K. Kawaguchi, J. Chem. Soc., Chem. Commun. **1991**, 1265 (1991).

[4] K. Murata, H. Ushijima, H. Ueda, and K. Kawaguchi, J. Chem.

Soc., Chem. Commun. **1992**, 567 (1992).
[5] K. Tanaka, M. Kobashi, H. Sanekata, A. Takata, T. Yamabe, S. Mizogami, K. Kawabata, and J. Yamauchi, J. Appl. Phys. **71**, 836 (1992).
[6] J. S. Miller, Adv. Mater. (Weinheim, Ger.) **4**, 435 (1992).
[7] T. L. Makarova, B. Sundqvist, R. Hohne, P. Esquinazi, Y. Kopelevich, P. Scharff, V. Davydov, L. S. Kashevarova, and A. V. Rakhmanina, Nature (London) **440**, 707 (2006).
[8] T. L. Makarova, B. Sundqvist, R. Hohne, P. Esquinazi, Y. Kopelevich, P. Scharff, V. A. Davydov, L. S. Kashevarova, and A. V. Rakhmanina, Nature (London) **413**, 716 (2001).
[9] R. Hohne and P. Esquinazi, Adv. Mater. (Weinheim, Ger.) **14**, 753 (2002).
[10] D. Spemann, K. H. Han, R. Hohne, T. L. Makarova, P. Esquinazi, and T. Butz, Nucl. Instrum. Methods Phys. Res. B **210**, 531 (2003).
[11] K. H. Han, D. Spemann, R. Hohne, A. Setzer, T. Makarova, P. Esquinazi, and T. Butz, Carbon **41**, 785 (2003).
[12] P. M. Allemand, K. C. Khemani, A. Koch, F. Wudl, K. Holczer, S. Donovan, G. Gruner, and J. D. Thompson, Science **253**, 301 (1991).
[13] B. Narymbetov, A. Omerzu, V. V. Kabanov, M. Tokumoto, H. Kobayashi, and D. Mihailovic, Nature (London) **407**, 883 (2000).
[14] A. Mrzel, A. Omerzu, P. Umek, D. Mihailovic, Z. Jaglicic, and Z. Trontelj, Chem. Phys. Lett. **298**, 329 (1998).
[15] Y. Murakami and H. Suematsu, Pure Appl. Chem. **68**, 1463 (1996).
[16] D. Spemann, K. H. Han, P. Esquinazi, R. Hohne, and T. Butz, Nucl. Instrum. Methods Phys. Res. B **219-220**, 886 (2004).
[17] P. O. Lehtinen, A. S. Foster, Y. Ma, A. V. Krasheninnikov, and R. M. Nieminen, Phys. Rev. Lett. **93**, 187202 (2004).
[18] K. H. Han, D. Spemann, P. Esquinazi, R. Hohne, V. Riede, and T. Butz, J. Magn. Magn. Mater. **272-276**, 1190 (2004), part 2, special issue SI.
[19] P. Esquinazi, R. Hohne, K. H. Han, A. Setzer, D. Spemann, and T. Butz, Carbon **42**, 1213 (2004).
[20] K. H. Han, D. Spemann, P. Esquinazi, R. Hohne, V. Riede, and T. Butz, Adv. Mater. (Weinheim, Ger.) **15**, 1719 (2003).
[21] K. Harigaya and T. Enoki, Mol. Cryst. Liq. Cryst. Sci. Technol., Sect. A **386**, 205 (2002).
[22] T. Enoki, N. Kawatsu, Y. Shibayama, H. Sato, R. Kobori, S. Maruyama, and K. Kaneko, Polyhedron **20**, 1311 (2001).
[23] K. Kusakabe and Y. Takagi, Mol. Cryst. Liq. Cryst. Sci. Technol., Sect. A **387**, 231 (2002).
[24] K. Kusakabe and M. Maruyama, Phys. Rev. B **67**, 092406 (2003).
[25] M. Maruyama, K. Kusakabe, S. Tsuneyuki, K. Akagi, Y. Yoshimoto, and J. Yamauchi, J. Phys. Chem. Solids **65**, 119 (2004).
[26] A. W. Mombru, H. Pardo, R. Faccio, O. F. de Lima, E. R. Leite, G. Zanelatto, A. J. C. Lanfredi, C. A. Cardoso, and F. M. Araujo-Moreira, Phys. Rev. B **71**, 100404(R) (2005).
[27] A. V. Rode, R. G. Elliman, E. G. Gamaly, A. I. Veinger, A. G. Christy, S. T. Hyde, and B. Luther-Davies, Appl. Surf. Sci. **197**, 644 (2002).
[28] N. Park, M. Yoon, S. Berber, J. Ihm, E. Osawa, and D. Tomanek, Phys. Rev. Lett. **91**, 237204 (2003).
[29] A. V. Rode, E. G. Gamaly, A. G. Christy, J. G. Fitz Gerald, S. T. Hyde, R. G. Elliman, B. Luther-Davies, A. I. Veinger, J. Androulakis, and J. Giapintzakis, Phys. Rev. B **70**, 054407 (2004).
[30] J. A. Rodriguez-Manzo, F. Lopez-Urias, M. Terrones, and H. Terrones, Nano Lett. **4**, 2179 (2004).
[31] H. Terrones, M. Terrones, F. Lopez-Urias, J. A. Rodriguez-Manzo, and A. L. Mackay, Philos. Trans. R. Soc. London, Ser. A **362**, 2039 (2004).
[32] T. L. Makarova, K. H. Han, P. Esquinazi, R. R. da Silva, Y. Kopelevich, I. B. Zakharova, and B. Sundqvist, Carbon **41**, 1575 (2003).
[33] V. E. Antonov, I. O. Bashkin, S. S. Khasanov, A. P. Moravsky, Y. G. Morozov, Y. M. Shulga, Y. A. Ossipyan, and E. G. Ponyatovsky, J. Alloys Compd. **330**, 365 (2002).
[34] R. A. Wood, M. H. Lewis, M. R. Lees, S. M. Bennington, M. G. Cain, and N. Kitamura, J. Phys.: Condens. Matter **14**, L385 (2002).
[35] A. N. Andriotis, M. Menon, R. M. Sheetz, and L. Chernozatonskii, Phys. Rev. Lett. **90**, 026801 (2003).
[36] D. W. Boukhvalov, P. F. Karimov, E. Z. Kurmaev, T. Hamilton, A. Moewes, L. D. Finkelstein, M. I. Katsnelson, V. A. Davydov, A. V. Rakhmanina, T. L. Makarova, *et al.* Phys. Rev. B **69**, 115425 (2004).
[37] Y. Kopelevich, R. R. daSilva, J. H. S. Torres, A. Penicaud, and T. Kvotani, Phys. Rev. B **68**, 092408 (2003).
[38] S. Bandow, F. Kokai, K. Takahashi, M. Yudasaka, and S. Iijima, Appl. Phys. A: Mater. Sci. Process. **73**, 281 (2001).
[39] S. Bandow, T. Yamaguchi, and S. Iijima, Chem. Phys. Lett. **401**, 380 (2005).
[40] L. R. Radovic and B. Bockrath, J. Am. Chem. Soc. **127**, 5917 (2005).
[41] J. Giles, news@nature.com
[42] P. Esquinazi, A. Setzer, R. Hohne, C. Semmelhack, Y. Kopelevich, D. Spemann, T. Butz, B. Kohlstrunk, and M. Losche, Phys. Rev. B **66**, 024429 (2002).
[43] G. C. DeFotis, Phys. Rev. B **23**, 4714 (1981).
[44] G. D. Morris, J. H. Brewer, S. R. Dunsiger, and M. Montour, Hyperfine Interact. **104**, 381 (1997).
[45] J. B. Goodenough, Phys. Rev. **100**, 564 (1955).
[46] J. L. Elechiguerra, J. L. Burt, J. R. Morones, A. Camacho-Bragado, X. Gao, H. H. Lara, and M. J. Yacaman, J. Nanobiotechnol. 3 (2005), online journal.
[47] Nanotechnologies, Inc. (now NovaCentrix), 1908 Kramer Lane, Building B, Austin, Texas, 78758, USA.